

HIGH-RESOLUTION X-RAY SPECTROSCOPY OF SNR 1987A: CHANDRA LETG AND HETG OBSERVATIONS IN 2007

SVETOZAR A. ZHEKOV^{1,5}, RICHARD MCCRAY¹, DANIEL DEWEY², CLAUDE R. CANIZARES², KAZIMIERZ J. BORKOWSKI³, DAVID N. BURROWS⁴, AND SANGWOOK PARK⁴

¹ JILA, University of Colorado, Boulder, CO 80309-0440, USA; zhekovs@colorado.edu, dick@jila.colorado.edu

² MIT, Kavli Institute, Cambridge, MA 02139, USA; dd@space.mit.edu, crc@space.mit.edu

³ Department of Physics, NCSU, Raleigh, NC 27695-8202, USA; kborkow@unity.ncsu.edu

⁴ Department of Astronomy and Astrophysics, Pennsylvania State University, 525 Davey Laboratory, University Park, PA 16802, USA; burrows@astro.psu.edu, park@astro.psu.edu

Received 2008 April 15; accepted 2008 October 29; published 2009 February 23

ABSTRACT

We present an extended analysis of the deep *Chandra* LETG and HETG observations of the supernova remnant 1987A (SNR 1987A) carried out in 2007. The global fits to the grating spectra show that the temperature of the X-ray emitting plasma in the slower shocks in this system has remained stable for the last three years, while that in the faster shocks has decreased. This temperature evolution is confirmed by the first light curves of strong X-ray emission lines and their ratios. On the other hand, bulk gas velocities inferred from the X-ray line profiles are too low to account for the postshock plasma temperatures inferred from spectral fits. This suggests that the X-ray emission comes from gas that has been shocked twice, first by the blast wave and again by shocks reflected from the inner ring of SNR 1987A. A new model that takes these considerations into account gives support to this physical picture.

Key words: supernova remnants – supernovae: individual (SNR 1987A) – X-rays: ISM

1. INTRODUCTION

Since its appearance on 1987 February 23, SN 1987A has passed through various stages of its evolution, and it is now well into the supernova remnant (SNR) phase (McCray 2007). Its reappearance in radio (Staveley-Smith et al. 1992, 1993) and in X-rays (Beuermann et al. 1994; Gorenstein et al. 1994; Hasinger et al. 1996) at ~ 1200 days after the explosion marked the beginning of this evolutionary phase. Since then it has been continuously brightening in X-rays, at an accelerating rate in the past few years (Park et al. 2005, 2006, 2007). On day 6067, Bouchet et al. (2004; see also Bouchet et al. 2006) obtained a 10 μm image of the remnant which has similar morphology to the X-ray image. X-ray observations are crucial for understanding the underlying physics of this phase because they manifest most of the energetics at present. Detailed X-ray spectral information deduced from grating observations provides us with essential information about the shocked plasma: its temperature; bulk gas velocity; chemical composition; etc.

Continuous brightening of SNR 1987A in the last decade has enabled spectral observations to be carried out with steadily improving photon statistics. The first such observations were performed with the High Energy Transmission Grating (HETG) aboard *Chandra* in 1999 October (Michael et al. 2002). Although the dispersed spectra contained relatively few source counts (602 in MEG and 255 in HEG), emission lines of thermal origin were clearly detected. Since then, dispersed spectra of SNR 1987A have been obtained in several observations: 2003 May (*XMM-Newton*; Haberl et al. 2006); 2004 August–September (*Chandra* Low Energy Transmission Grating (LETG); Zhekov et al. 2005, 2006, hereafter Z05, Z06); 2007 January (*XMM-Newton*; Heng et al. 2008); 2007 March–April (*Chandra* HETG; Dewey et al. 2008, hereafter D08); and 2007 September (*Chandra* LETG; this work).

The superb spatial and spectral resolution of the *Chandra* observatory opens new possibilities for studying SNR 1987A. The grating observations provide us not only with details about the thermodynamics and kinetics of the X-ray emitting gas but also about its geometry. For example, the analysis of the first LETG observations with good photon statistics (Z05) demonstrated that the X-ray emission region is an expanding ring, having geometry similar to optical image of the inner ring in SNR 1987A as seen with the *Hubble Space Telescope*. This conclusion was confirmed by data from more recent *Chandra* HETG observations (D08). In fact, this conclusion was suggested by the similarity between the optical and X-ray images (e.g., Burrows et al. 2000; Park et al. 2004, 2006), but one could not rule out a more nearly spherical geometry from the X-ray images alone.

Here we present an extended analysis of the HETG and LETG grating observations of SNR 1987A that were carried out with *Chandra* in 2007. D08 have already reported the first part of our analysis, which focused mainly on the HETG data. For the current analysis, we assume that the X-ray emitting plasma distribution is symmetric about the axis of the inner circumstellar ring. This assumption is clearly not true, as can be seen from the X-ray images (Park et al. 2004, 2006), but we adopt it here as a first approximation, as we did with the LETG 2004 data, in order to see how the inferred parameters change with time. In this study, we also carry on a detailed comparison between the techniques used so far for deriving parameters of the strong lines in the X-ray spectrum of SNR 1987A. This relates in a more transparent way the results obtained with different instrumentations. The better constrained observational facts are a good basis for a more elaborated interpretation as well.

This paper is organized as follows. In Section 2, we briefly review the X-ray observations. In Section 3, we present models for the emitting gas, which are based on global fits to the entire spectrum of SNR 1987A. In Section 4, we analyze the profiles and ratios of strong X-ray emission lines. In Section 5, we report results from the two-dimensional analysis of the X-ray

⁵ On leave from Space Research Institute, Sofia, Bulgaria.

observations. In Section 6, we discuss the physical picture that emerges from analysis of current and previous data. Finally, in Section 7, we list our conclusions.

2. OBSERVATIONS AND DATA REDUCTION

In 2007, SNR 1987A was observed with both the grating spectrometers aboard *Chandra*: HETG and LETG. The observations in configuration LETG-ACIS-S were carried out in nine consecutive sequences (*Chandra* ObsIDs: 7620, 7621, 9580, 9581, 9582, 9589, 9590, 9591, and 9592) that took place between 2007 September 4 and September 16 (7498–7510 days after the explosion) and provided a total effective exposure of 285 ks. The roll angle was between 95° and 98°; therefore, the dispersion axis was aligned approximately with the minor axis (north–south) of the inner ring in SNR 1987A (P.A. \approx 354°; Sugerman et al. 2002).

The positive and negative first-order LETG spectra for each of the nine observations were extracted following the Science Threads for Grating Spectroscopy in the CIAO 3.4 data analysis software.⁶ The resultant spectra were merged into one spectrum each for the positive and negative LETG arms with respective total counts of 23,797 (LETG + 1) and 15,358 (LETG – 1). The ancillary response functions for all spectra were generated using the *Chandra* calibration database CALDB v.4.0 (the terms LETG and LEG will be used throughout the text to refer to the LETG data and spectra).

We discussed the 2007 HETG data of SNR 1987A in D08; here we only recall that the first-order spectra contain the following numbers of counts: 15,200 (MEG – 1); 14,000 (MEG + 1); 5800 (HEG – 1); and 4700 (HEG + 1).

Finally, the instrument configurations were such that the *negative* first-order LEG arm was pointing to north, and the same was true for the *positive* first-order MEG/HEG arm. Anticipating the discussion of the spatial-spectral effects, we note that the narrowed (“compressed”) spectral lines are thus found in their corresponding spectra (LEG – 1; MEG/HEG + 1).

Figure 1 displays portions of these spectra in the vicinity of strong emission lines. The superior spectral resolution of the MEG is evident in the emission line profiles.

3. GLOBAL FITS

We performed global fits following the procedure we used to analyze the 2004 LETG spectra (Z06; details of the global models are found therein). We considered two basic models: (1) a two-shock model and (2) a DS-shock model (distribution of shocks). In all the cases, we constructed simultaneous model fits to six background-subtracted (positive and negative first-order) spectra of LETG 2004, HETG 2007 (MEG), and LETG 2007. We rebinned all spectra to ensure a minimum of 30 counts per bin. The basic assumptions of our models are outlined in Section 3.1 and the results are given in Section 3.2.

3.1. Basic Assumptions

In our global analysis we fit our data to a model consisting of a distribution of plane-parallel strong adiabatic (index $\gamma = 5/3$) shocks with velocity V_{sh} that enter stationary gas. Therefore, the postshock gas velocity is $V_{\text{psh}} = (3/4)V_{\text{sh}}$. Given the adopted set of abundances (see Z06 and below), the mean molecular weight

per particle is $\mu = 0.72$; thus the postshock temperature is

$$kT = 1.4(V_{\text{sh}}/1000 \text{ km s}^{-1})^2 \text{ keV}. \quad (1)$$

We model the X-ray spectrum of the shocked plasma taking into account the effects of nonequilibrium ionization (NEI), by using either the corresponding models in XSPEC (*vpshock* in version 11.3.2; Arnaud 1996) that are based on Borkowski et al. (2001) or custom XSPEC models constructed on the same basis (Z06). In fitting models consisting of a distribution of shocks, we take as the basic “vectors” plane-parallel strong adiabatic shocks characterized by their postshock temperature and emission measure. The NEI effects are characterized by the “ionization age,” ($n_e t$), i.e., the product of the postshock electron number density and time since shock passage.

In our global fits we assume that all spectra share the same value, N_H , of the interstellar absorption, which does not change with time.

Likewise, we assume that the chemical abundances of the hot (shock-heated) plasma are constant over time. To determine them, we adopted the same procedure as in our previous spectral analyses (Michael et al. 2002; Park et al. 2002, 2004, 2006; Z06; D08). That is, we only varied the abundances of elements having strong emission lines in the observed (0.5–4 keV) energy range: N, O, Ne, Mg, Si, S, and Fe. We held the abundances of H, He, C, Ar, Ca, and Ni fixed to their corresponding values as discussed originally in Michael et al. (2002). Some evolution of the chemical composition might take place due to destruction of dust grains when the shocks engulf the denser parts of the equatorial disk. But we find at most modest depletions of refractory elements in the X-ray emitting gas and neglect dust destruction effects in the present work (see also Section 3.2).

3.2. Fit Results

Table 1 displays results from our simultaneous two-shock model fit to the LEG 2004, MEG 2007 and LEG 2007 spectra of SNR 1987A. We note that the shock parameters in 2004 from the simultaneous fit are very close to those derived from the LETG 2004 analysis alone (Z06), which makes us confident about the model assumptions listed in Section 3.1. Also, we see a gradual increase in the shock ionization ages which is natural to expect if the blast wave encounters gas of increasing density as it propagates into the circumstellar ring.

We also constructed a simultaneous fit ($\chi^2/\text{dof} = 1789/2242$) of all the data with the distribution of shocks model and inferred the following values (with 1σ errors) for absorption column density and elemental abundances (as ratios to their solar values, Anders & Grevesse 1989): $N_H = 1.44 \pm 0.01 \times 10^{21} \text{ cm}^{-2}$; N = 0.73 ± 0.07 ; O = 0.10 ± 0.01 ; Ne = 0.34 ± 0.01 ; Mg = 0.31 ± 0.01 ; Si = 0.37 ± 0.01 ; S = 0.33 ± 0.04 ; and Fe = 0.20 ± 0.01 . Note that these results are close both to the values given in Table 1 and to those from the LETG 2004 DS analysis.

Figure 2 displays the distributions of emission measures and ionization ages inferred from DS model fits to the LEG 2004, MEG 2007, and LEG 2007 spectra. The figure shows that the shock distribution is quite stable over a period of three years, especially in its soft part. On the other hand, we do see noticeable evidence of a change in the high-temperature tail. This result is consistent with the results we infer from a two-shock model fit to the spectra (Table 1). The fact that the shape of the shock distribution is almost the same for the HETG (MEG) 2007 and LETG 2007 data sets gives us confidence that our

⁶ *Chandra* Interactive Analysis of Observations (CIAO), <http://cxc.harvard.edu/ciao/>.

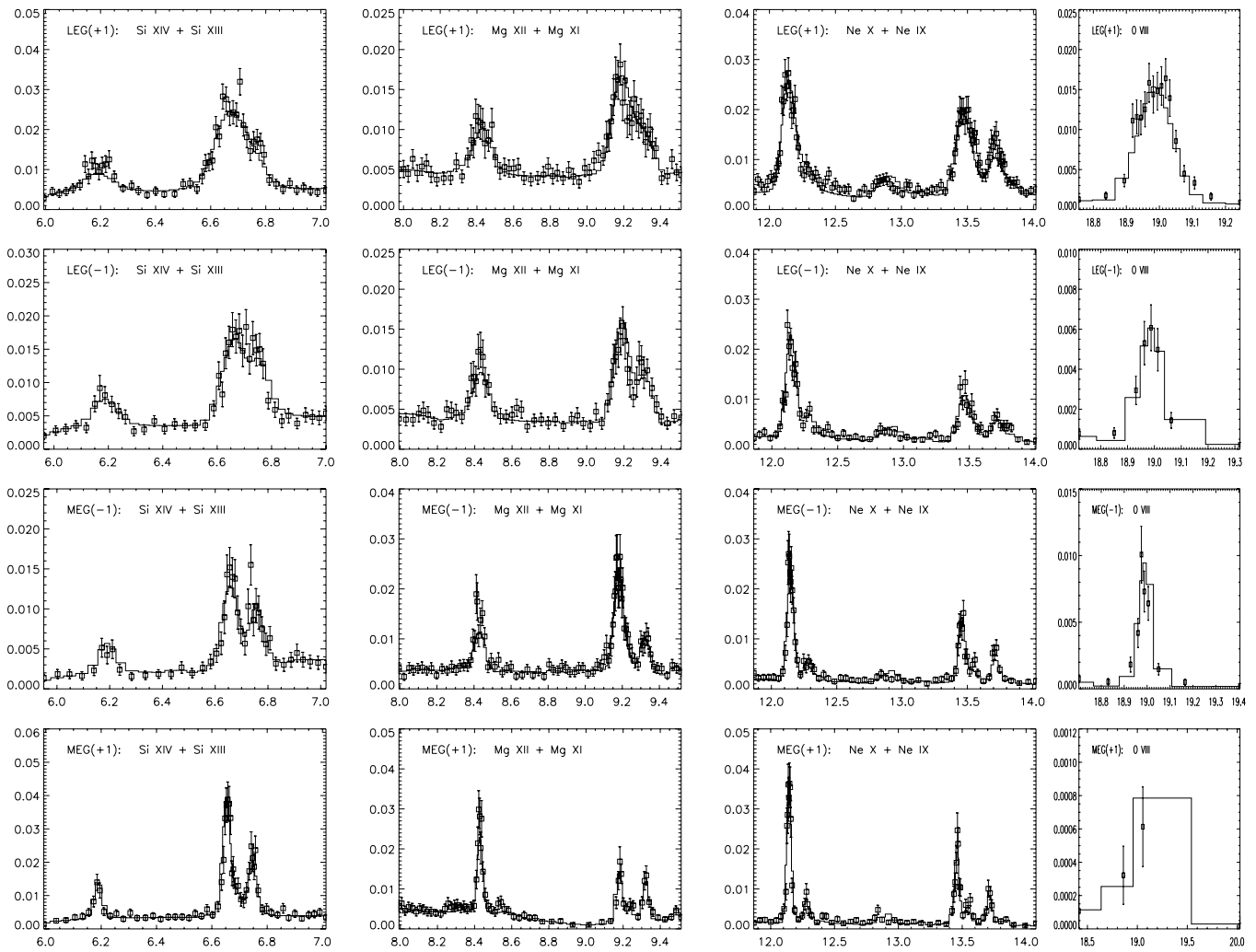


Figure 1. X-ray spectra of SNR 1987A in 2007 near the strong spectral lines of the ions Si xiv, Si xiii, Mg xii, Mg xi, Ne x, Ne ix and O viii: (1) empty squares with 1σ error bars: observed spectra; (2) solid curves: the theoretical spectra from the two-shock model. Horizontal axes:- observed wavelength (\AA); vertical axes: flux density ($\text{photons s}^{-1} \text{\AA}^{-1}$). The positive and negative LEG first-order data are shown in the first and second row, respectively. The negative and positive MEG first-order data are shown in the third and fourth row, respectively. All observed spectra are rebinned to have a minimum of 30 counts per bin. For the 2004 LEG spectra see Figure 2 in Z06.

DS analysis procedure is robust with regard to the instrument spectral resolution.

Unfortunately, it is not feasible for us to carry out a detailed error analysis for the DS shape. The parameter space is too large and the CPU time requirements would be prohibitive. Instead, we performed the standard F -test that shows whether the derived distributions have significantly different variances. We note that the variance is a conventional measure of the “width,” that is of the shape, of a given distribution. The results of the F -test show that the probability of the null hypothesis (or of “identical” shapes) is: 0.006 for LEG 2004 and LEG 2007 data; 0.01 for LEG 2004 and MEG 2004; and 0.85 for LEG 2007 and MEG 2007. Therefore, we conclude that the slight change in the shape of the shock distribution from MEG 2007 to LEG 2007 is visually suggestive but not statistically significant, whereas there is clear significance to the change in the three-year interval between the LEG 2004 observation and the LEG 2007 observation.

Inspecting the results from our shock fits (Table 1 and Figure 2), we note the following points.

The abundances of SNR 1987A derived from analysis of the entire set of grating spectra taken so far with *Chandra* confirm

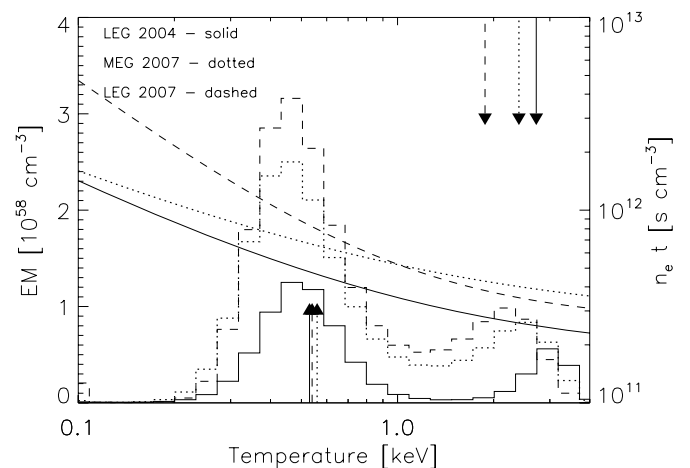


Figure 2. Emission measure (EM) of the distribution of shocks in SNR 1987A as derived from the DS model with 25 points logarithmically spaced in the (0.1–4 keV) postshock temperature range. The arrows indicate the postshock temperature from the two-shock model fits (see Table 1): low (high)-temperature components are plotted from the lower (upper) x -axis. The smooth lines show the derived ionization age of each shock ($n_e t$).

Table 1
Two-Shock Model Results (First-Order Spectra)

Parameters	LEG 2004	MEG 2007	LEG 2007
χ^2/dof	...	1819/2248	...
N_H (10^{21} cm $^{-2}$)	...	1.30 [1.18–1.46]	...
kT_1 (keV)	0.53 [0.50–0.55]	0.56 [0.53–0.59]	0.54 [0.53–0.56]
kT_2 (keV)	2.70 [2.54–3.03]	2.43 [1.94–2.72]	1.90 [1.84–1.97]
τ_1^a	3.20 [2.63–4.30]	3.63 [3.33–4.58]	4.78 [4.06–5.88]
τ_2^a	1.58 [1.23–2.13]	2.23 [1.81–2.76]	2.67 [2.23–3.25]
EM $_1^b$	4.12	9.12	10.9
EM $_2^b$	1.71	4.22	5.63
H	1	1	1
He(2.57)	2.57	2.57	2.57
C(0.09)	0.09	0.09	0.09
N(1.63)	...	0.56 [0.50–0.65]	...
O(0.18)	...	0.081 [0.074–0.092]	...
Ne(0.29)	...	0.29 [0.27–0.31]	...
Mg(0.32)	...	0.28 [0.26–0.29]	...
Si(0.31)	...	0.33 [0.32–0.35]	...
S(0.36)	...	0.30 [0.24–0.36]	...
Ar	0.537	0.537	0.537
Ca	0.339	0.339	0.339
Fe(0.22)	...	0.19 [0.19–0.21]	...
Ni	0.618	0.618	0.618
F_X^c (0.5–2 keV)	1.48 [1.37–1.56]	3.27 [3.14–3.40]	3.84 [3.70–3.96]
F_X^c (0.5–6 keV)	1.84 [1.68–1.94]	4.08 [3.80–4.21]	4.65 [4.48–4.78]

Notes. Results from the *simultaneous* fit to the LETG 2004, MEG 2007 and LEG 2007 spectra. 90% confidence intervals are given in brackets, and all abundances are expressed as ratios to their solar values (Anders & Grevesse 1989). For comparison, the inner-ring abundances of He, C, N, and O (Lundqvist & Fransson 1996); those of Ne, Mg, Si, S, and Fe typical for LMC (Russel & Dopita 1992) are given in the first column in parentheses.

^a ($n_e t$) in units of 10^{11} cm $^{-3}$ s.

^b $EM = \int n_e n_H dV$ in units of 10^{58} cm $^{-3}$ if a distance of 50 kpc is adopted.

^c The observed X-ray flux in units of 10^{-12} ergs cm $^{-2}$ s $^{-1}$.

the conclusions from our previous analysis (Z06). Namely, Ne, Mg, Si, S, and Fe have abundance values typical for the LMC (Russel & Dopita 1992), while N and O abundances derived from the X-ray spectra are a factor of ~ 2 lower than those found by Lundqvist & Fransson (1996) from optical and UV spectra of the inner ring. The lower nitrogen abundance found here is in accord with the value inferred by Pun et al. (2002) from their analysis of the optical and UV spectra of Spot 1 on the inner circumstellar ring.

The gas-phase abundance of silicon measured from the X-ray spectrum is of particular interest because it places constraints on the depletion of silicon onto dust grains in the circumstellar matter and on the destruction of the dust grains in the X-ray emitting gas (Dwek et al 2008). As seen from Table 1, the silicon abundance in the X-ray emitting region has a value typical for LMC. This fact implies either that there was little silicon depletion in the circumstellar ring or that most of the dust in the X-ray emitting gas has been vaporized. This result is consistent with an earlier analysis of the first mid-IR spectrum of SNR 1987A (Bouchet et al. 2006), which concluded that the dust-to-gas ratio in the inner ring of SNR 1987A is considerably lower than that for the interstellar medium in the LMC (i.e., no Si depletion in the gas phase). But in a recent and more elaborate analysis, Dwek et al. (2008) found that the mid-IR emission of the circumstellar ring can be explained if a dust abundance typical for the interstellar medium in LMC is adopted. Dwek et al. also found that the ratio of infrared to X-ray emission

decreased from day 6190 to 7137 and interpreted this evolution as evidence that dust grains were being destroyed by sputtering in the X-ray emitting gas. If so, one might expect to see a secular increase of the abundance of silicon in the X-ray spectrum; but we do not see evidence for such an increase. The values of silicon abundance derived from analysis of different X-ray spectra of SNR 1987A with good photon statistics are consistent with each other and with the value typical for LMC (Si = 0.31; Russel & Dopita 1992); Si = 0.30 ± 0.1 (1σ error from CCD spectra; Michael et al. 2002); Si = 0.32 ± 0.07 (1σ error from CCD spectra; Park et al. 2004); Si = 0.28 (0.22–0.32, 90% confidence interval from grating spectra; Z06); Si = 0.33 (0.32–0.35; 90% confidence interval from grating spectra; this work). Thus, we can rule out an increase of the gas-phase silicon abundance by a factor greater than $\sim 30\%$ in the period 2002–2007. These constraints on the physical processes governing the evolution of the shocked dust deserve a more detailed analysis than we intend to provide in this paper. Such an analysis should take account of uncertainties in the grain size distribution; temperature stratification of the X-ray emitting plasma (see Figure 2); uncertainties in the unabsorbed X-ray flux, etc. Obviously, these results are tantalizing and suggest that future observations both in X-rays and mid-IR and more elaborate, joint modeling of these spectra will tell us much about dust destruction in SNR 1987A.

The cooling trend for the shocked-heated plasma in SNR 1987A that we infer from both the two-temperature model and the DS model fits to the grating data is consistent with the trend inferred from fits to the pulse height spectra of the imaging data (Park et al. 2006). We believe that the trend is a result of the fact that the blast wave is encountering gas of increasing density as it enters the inner ring. The inferred evolution of the shock ionization age, although not a very tightly constrained parameter, is consistent with this conclusion. It is worth noting that the X-ray plasma models assumed a complete adiabaticity. Such an assumption is likely to break when the blast wave reaches deep in the inner ring, and a more elaborate modeling will be required that also takes into account the efficient hot gas cooling due to dust emission.

The actual distributions of densities, velocities, and temperatures, and ionization ages of the X-ray emitting gas in SNR 1987A are likely to be very complex. The model fits to global spectra presented here are surely oversimplified and miss many details; but we believe that they provide insight into the actual situation. The two-shock models give us an idea of the temperature trends of the shock distribution, while the DS models provide a bit more detail of the temperature distribution function. The main advantage of these models is that they take into account the NEI. But to begin to understand how the temperature distribution of the shocked gas is related to the actual hydrodynamics and geometry of the shock interaction region, we need to analyze line profiles.

4. SPECTRAL LINES: PROFILES, RATIOS, AND LIGHT CURVES

The widths and ratios of spectral lines can provide us with additional diagnostics of the shocked gas. For example, the evolution of the ratios of lines from particular ions indicates the temperature evolution of the plasma that emits these lines and the importance of NEI. On the other hand, the line profiles give us a measure of the bulk velocity, V_{bulk} , of the X-ray emitting plasma. It is interesting to compare the velocities inferred from line profiles with the velocity of the shocked gas inferred from

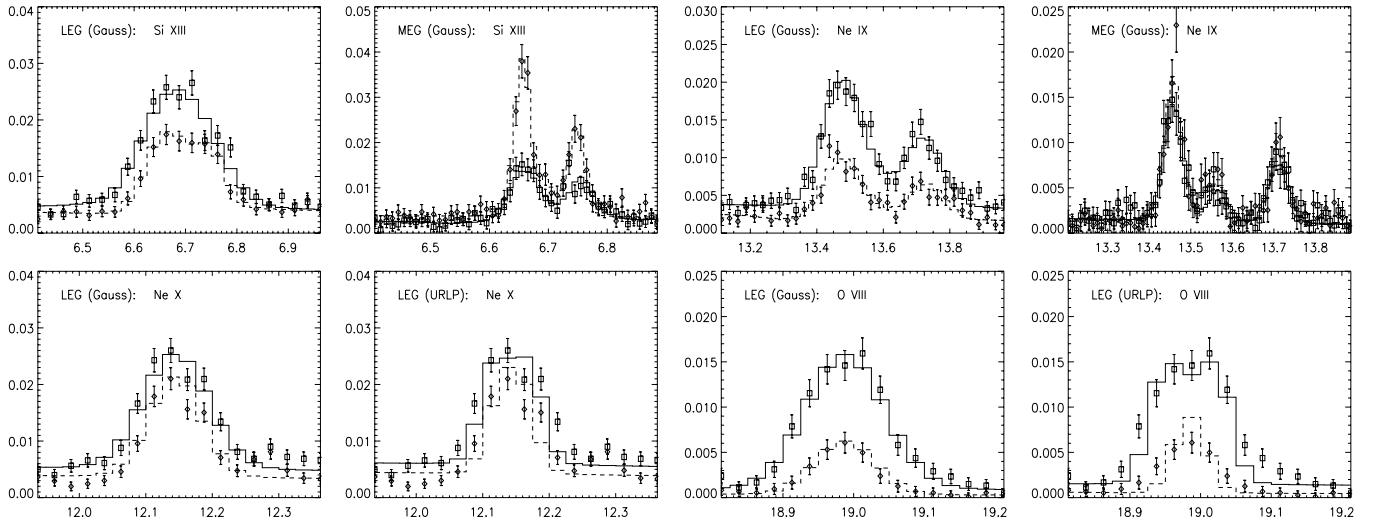


Figure 3. Examples of fits to the line profile of some strong lines in the X-ray spectra of SNR 1987A in 2007. The first row presents the He-like triplets of Si XIII and Ne IX for the LEG and MEG spectra, assuming that each component has Gaussian profile. The second row shows the H-like doublets of Ne X and O VIII as detected in the LEG spectra. Both Gaussian and uniform-ring line profile (URLP) models were used in the fits. The broadened (LEG+1; MEG−1) and narrowed (LEG−1; MEG+1) lines are shown by solid and dashed stepped lines, respectively. Horizontal axes; observed wavelength (Å); vertical axes; flux density (photons $s^{-1} \text{Å}^{-1}$).

its temperature according to Equation (1). Two cases are worth noting:

1. $V_{\text{bulk}} > (3/4)V_{\text{sh}}$, in which case the explanation could be: (1) the ion and electron temperatures behind the shock have not equilibrated yet or (2) the shocks are oblique.
2. $V_{\text{bulk}} < (3/4)V_{\text{sh}}$, in which case the most likely explanation is that reflected shocks are the dominant source of heat for the X-ray emitting plasma.

4.1. Line Profile Fitting

A general and very important feature of the line profile analysis of the *Chandra* X-ray grating spectra of SNR 1987A is that due to the complex nature of the spatial-spectral effects, we cannot measure directly the bulk gas velocities in the hot plasma. In fact, we can measure the line widths; but to infer the bulk gas velocities, we must carry on some modeling as well. Two approaches have been adopted so far: (1) Z05 derived the widths of individual spectral lines in the positive and negative first-order spectra, which were then fitted simultaneously to deduce the gas velocities; (2) D08 used an expanding ring model to fit the line profiles and the gas velocities were derived for each spectral line. Both techniques were used in the present analysis of the 2007 HETG and LETG spectra. This approach served two purposes: first, to ensure compatibility with the 2004 LETG analysis; and, second, to better constrain the derived line parameters.

For the first technique, we follow the procedure employed by Z05, and we used a Gaussian fit to the line profiles. Having derived the line widths for the first-order spectra, we fit them by the formula that assumes that the net line width (FWHM) is

$$\Delta\lambda_{\text{tot}} = 2\Delta\lambda_0 \pm 2z_0(\lambda/\lambda_0)^\alpha \lambda, \quad (2)$$

where the plus (minus) sign refers to the (+1/−1) order of the LEG spectrum and to the (−1/+1) order of the MEG spectrum, respectively. In this simplified representation of the spatial-spectral effects, the first term accounts for the spatial broadening and the second term accounts for the bulk gas motion. The parameter z_0 determines the line broadening at some fiducial wavelength λ_0 . The coefficient α accounts for

velocity stratification of the shocked gas. If all spectral lines have the same bulk gas velocity, $\alpha = 0$; otherwise, $\alpha \neq 0$.

For the second technique, we constructed a custom model in XSPEC in which we assume that the line is emitted from a gas with uniform density and bulk gas velocity, occupying a ringlike structure. We call this model the “Uniform-Ring Line Profile” (URLP) model. Details are found in Appendix A. Examples of fits with the both techniques to spectral lines in the HETG 2007 and LEG 2007 spectra are given in Figure 3. At wavelengths smaller than $\approx 15 \text{Å}$, we fitted the HEG and MEG data simultaneously; otherwise we included only the MEG data.

Figure 4 shows the results of using the Gaussian technique that renders a comparison with the results from the LETG 2004 analysis. The derived FWHMs of strong emission lines clearly illustrate the spatial-spectral effects, namely, the line widths are broadened in one of the spectrograph’s arms, and they are narrowed in the other one. Also, the line widths are smaller in MEG spectra compared with those in the LEG spectra. This is a direct result of the different spectral scale (Å per arcsecond) in the two instruments with that of LEG being a factor ~ 2.5 larger. Therefore, the spatial broadening is larger in LEG (see the first term in Equation (2)), which translates to larger observed line widths. In the shock-stratified case, the best-fit values and the corresponding 1σ errors from the fits are: $\Delta\lambda_0 = 0.0207 \pm 0.0006 \text{Å}$, $z_0 = 0.00089 \pm 0.00005$, and $\alpha = -1.57 \pm 0.28$ (MEG 2007); $\Delta\lambda_0 = 0.0454 \pm 0.0012 \text{Å}$, $z_0 = 0.00061 \pm 0.00096$, and $\alpha = -1.06 \pm 0.46$ (LEG 2007). We note that given the grating dispersions of $0.056 \text{Å arcsec}^{-1}$ (LEG) and $0.0226 \text{Å arcsec}^{-1}$ (MEG), the derived values for the source “half-size” ($\Delta\lambda_0$) are consistent between MEG and LEG data: $0''.92$ and $0''.81$, respectively. The lower right-hand side panel in Figure 4 shows the derived shock stratification. The “error bars” indicate the confidence limits corresponding to the $\pm 1\sigma$ errors in the fits. Two things are immediately evident:

1. Despite the relatively large errors, the fast shock velocities in the distributions are slowing down (LEG 2004 versus LEG 2007). This is consistent with the temperature trend discussed in Section 3.

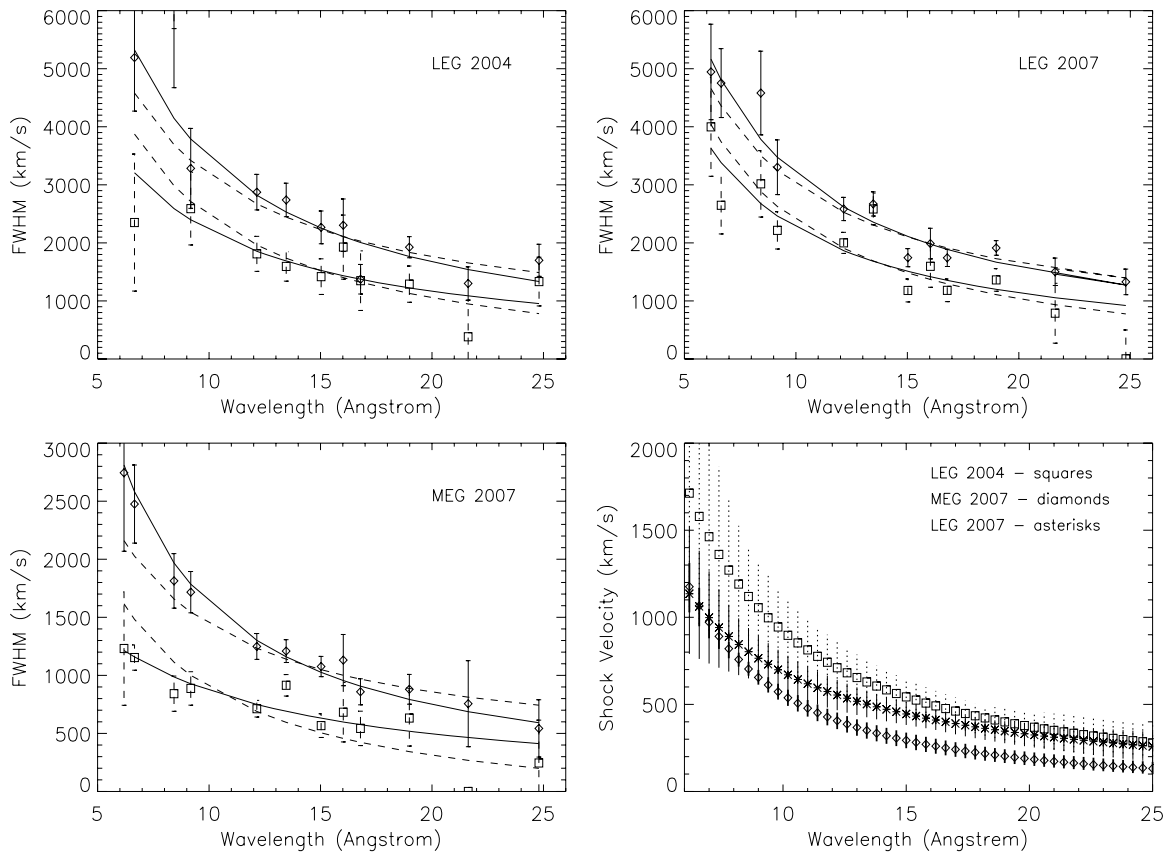


Figure 4. Measured line widths (FWHM) for the broadened (diamonds) and narrowed (squares) spectral arms, respectively. The solid and dashed curves correspond to the line broadening parameter in the cases with and without shock stratification (see Equation (2)). The lower right-hand panel shows the derived shock stratification. The “error bars” indicate the confidence limits corresponding to the $\pm 1\sigma$ errors in the fits. The LEG 2004 results are from Z05.

2. Although they are qualitatively consistent, the shock velocities inferred from the LEG data are greater than those derived from the MEG spectra (LEG 2007 versus MEG 2007).

We note that D08 already reported relatively low bulk gas velocities in SNR 1987A from an analysis of the HETG 2007 spectra based on a line-profile model that assumes a uniform gas motion and a ringlike geometry. Here, we arrive at the same conclusion by employing a completely different modeling technique.

Figure 5 and Table 2 compare some results from the application of the two techniques to the grating spectra in 2007 (HETG and LETG). The basic conclusions are as follows.

1. The line centroids show no apparent deviations from the redshift ($+286 \text{ km s}^{-1}$) of the Large Magellanic Cloud. Thus, there is no evolution of this parameter between 2004 and 2007.
2. The line fluxes determined from the Gaussian model are greater than those determined from the URLP model, typically by 20%–25%. This is probably due to the fact that the lines do not have wings in the URLP model. In fact, the fluxes derived here from the HETG 2007 data generally bracket the D08 values. This can be attributed to the fact that D08 also included additional Gaussian line broadening in their ring profile model, making it intermediate between a pure Gaussian and the URLP model.
3. In the HETG data, the “ G -ratios” ($G = (f + i)/r$, where f , i , and r stand for forbidden, intercombination, and

resonance line fluxes, respectively of the He-like triplets) determined from the Gaussian and URLP models agree very well. But with the LETG data, the two models give noticeably different G -ratios for some triplets. We believe that this fact is a consequence of the inferior spectral resolution of the LETG data.

4. On the other hand, the two models agree very well in determining ratios of K_{α}/Ly_{α} ratios both for the HETG and LETG spectra. These ratios are determined by well-separated emission lines for which spectral resolution is not a critical factor.

The bulk gas velocities derived from HETG 2007 data are somewhat lower than those derived from the LETG 2007 data, although for some lines the opposite is true. Since there are no drastic changes in the spectra in the interval between these observations (see also Figure 2), we doubt that this difference is real. Instead, we believe that the lower velocities determined from the HETG 2007 data are more accurate due to its better spectral resolution. This is particularly true for the He-like triplets at shorter wavelengths. On the other hand, at longer wavelengths ($\sim \lambda > 18 \text{ \AA}$) the LETG results should be preferable due to the better quality of the LETG spectra. In general, we believe that taken together the results from the two different techniques (lower right panel in Figure 5), bracket the bulk gas velocities in the X-ray emitting region of SNR 1987A in 2007. This is also supported by our MARX⁷ simulations. Namely, we simulated line emission from a ringlike structure

⁷ See <http://space.mit.edu/CXC/MARX/>.

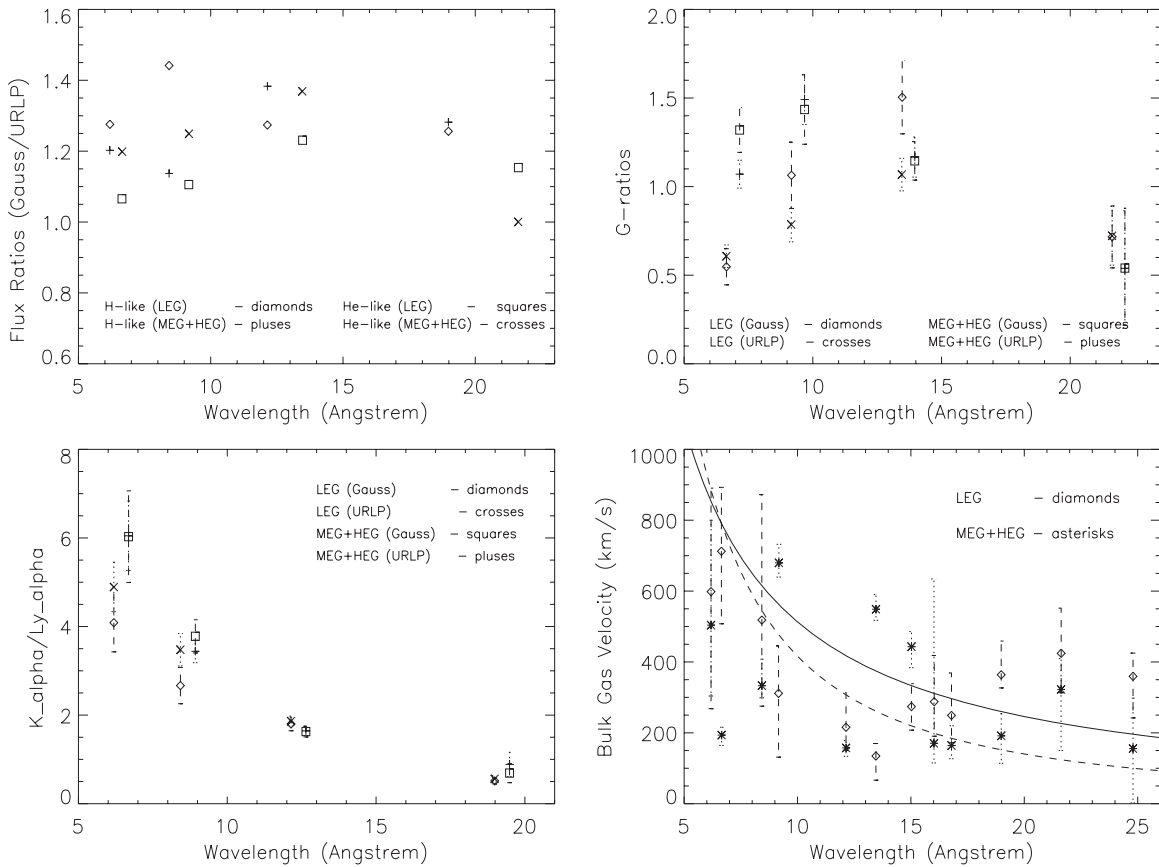


Figure 5. Comparisons between results from the Gaussian and URLP fits to the line profiles of the “major” emission lines in the 2007 X-ray spectrum of SNR 1987A (Si xiv 6.18 Å; Si xiii 6.65 Å; Mg xii 8.42 Å; Mg xi 9.17 Å; Ne x 12.13 Å; Ne ix 13.45 Å; O viii Ly α 18.97 Å; O vii 21.60 Å). Upper left: flux ratios. Upper right: the G-ratios (Si xiii; Mg xi; Ne ix; O vii); the data for the MEG + HEG are shifted by 0.5 Å for clarity. Lower left: the K_{α}/Ly_{α} ratios ([Si xiii/Si xii]; [Mg xi/Mg xii]; [Ne ix/Ne x]; [O viii/O viii]); the data for the MEG + HEG are shifted by 0.5 Å for clarity. Lower right: the derived bulk gas velocity from the URLP fits for all the strong lines in the spectra (additional to the listed above “major” lines are: Fe xvii doublet 15.01 Å and 15.26 Å; O viii Ly β 16.01 Å; Fe xvii triplet 16.78 Å, 17.05 Å and 17.10 Å; N vii 24.78 Å). For comparison, the solid and dashed lines show the shock stratification from Figure 4 (lower right panel) for LEG 2007 and MEG 2007, respectively, with bulk gas velocities equal to 3/4 of the shock velocities. In all these figures the notation MEG + HEG means that the MEG and HEG data for a spectral line were fitted simultaneously requiring the same line flux, bulk gas velocity, etc. This is done for all the lines with a wavelength smaller than 15.5 Å. The results for all other HETG lines are based only on the MEG spectra. Error bars correspond to the associated $\pm 1\sigma$ errors. No reddening correction has been applied to the line fluxes.

Table 2
SNR 1987A: Line Fluxes

Line	$\lambda_{\text{lab}}^{\text{a}}$ (Å)	LETG 2007 ^b		HETG 2007 ^b	
		Gauss	URLP	Gauss	URLP
Si xiv L α	6.1804	10.0 \pm 1.3	7.9 \pm 0.8	5.2 \pm 0.9	4.3 \pm 0.5
Si xiii K α	6.6479	41.0 \pm 3.7	38.5 \pm 2.2	31.4 \pm 1.5	26.2 \pm 1.0
Mg xii L α	8.4192	17.9 \pm 2.3	12.4 \pm 1.1	11.6 \pm 0.9	10.2 \pm 0.6
Mg xi K α	9.1687	47.7 \pm 4.2	43.2 \pm 2.7	43.7 \pm 2.8	35.0 \pm 1.6
Ne x L α	12.1321	92.9 \pm 5.4	72.9 \pm 5.4	82.4 \pm 4.8	60.0 \pm 2.6
Ne ix K α	13.4473	167.3 \pm 10.6	135.9 \pm 5.8	134.2 \pm 6.3	98.0 \pm 4.7
Fe xvii ^c	15.0140	93.7 \pm 5.5	86.9 \pm 3.6	88.5 \pm 4.7	78.4 \pm 3.8
O viii L β	16.0055	49.5 \pm 6.6	36.3 \pm 3.3	36.5 \pm 7.6	28.8 \pm 3.8
Fe xvii ^c	16.7800	135.0 \pm 10.3	123.4 \pm 9.3	111.2 \pm 9.3	98.4 \pm 9.0
O viii L α	18.9671	142.3 \pm 7.5	113.3 \pm 5.8	104.8 \pm 10.8	81.8 \pm 8.6
O vii K α	21.6015	73.2 \pm 8.9	63.4 \pm 7.4	72.5 \pm 21.5	72.5 \pm 21.0
N vii L α	24.7792	69.0 \pm 7.4	62.2 \pm 6.5	73.9 \pm 17.8	65.3 \pm 14.7

Notes.

^a The laboratory wavelength of the main component.

^b The observed total line/multiplet flux in units of 10^{-6} photons cm^{-2} s^{-1} and the associated 1σ errors for two different line profiles: Gaussian and URLP.

^c The total flux from the strongest component $\lambda\lambda 15.01, 15.26$ and $\lambda\lambda\lambda 16.78, 17.05, 17.10$ respectively.

with a uniform bulk gas velocity in the range (200–400) km s^{-1} at longer wavelengths (12.13 and 18.97 Å) and in the range

(400–800) km s^{-1} at short wavelengths (6.18 Å) for an SNR 1987A *Chandra* exposure of 300 ks. We extracted the MEG

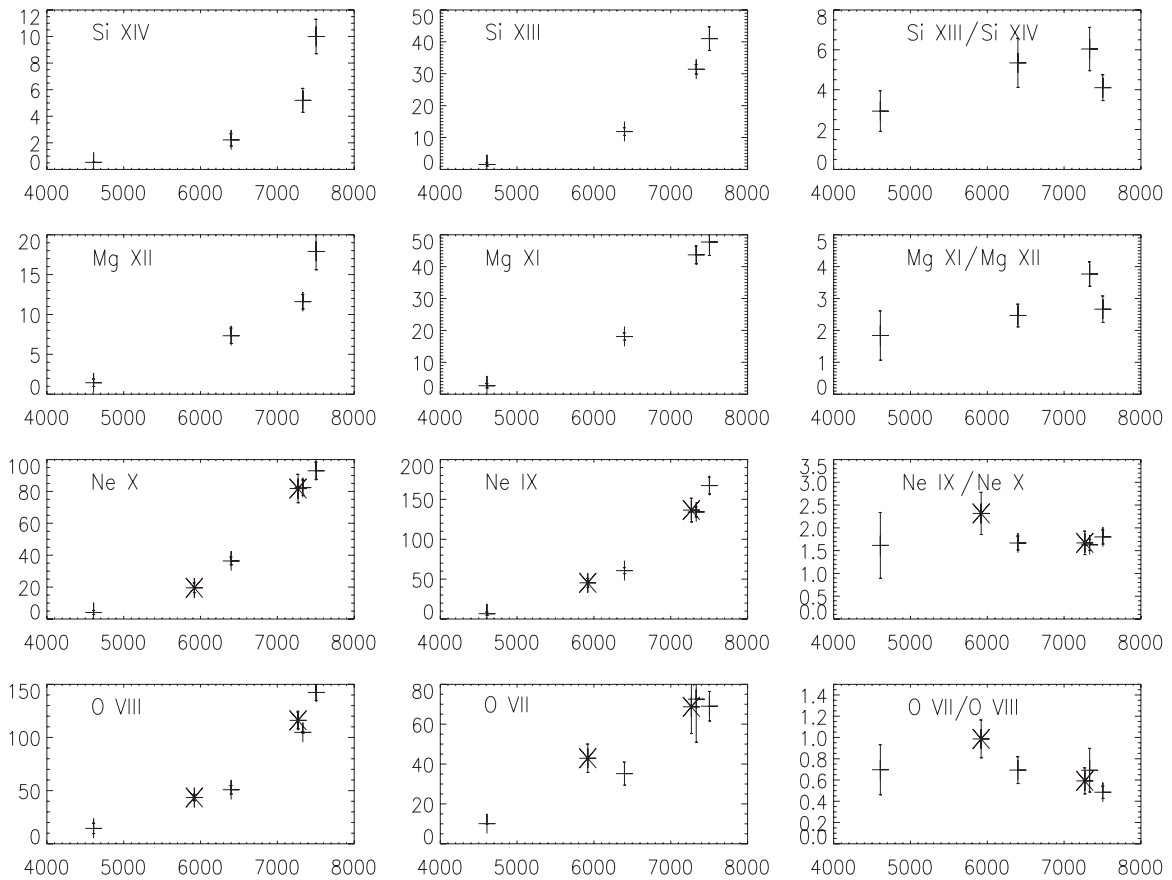


Figure 6. Light curves of some strong spectral lines in SNR 1987A. Plots in each row show consecutively the H-like Ly_{α} , He-like K_{α} and their ratio. Horizontal axes are the days after explosion; vertical axes (for the plots in the first and second columns) are observed line fluxes (10^{-6} photons $\text{cm}^{-2} \text{s}^{-1}$). The data points shown by pluses (and error bars) are for the *Chandra* gratings observations and are taken from Michael et al. (2002; for day 4608), Z05 (for day 6398) and Table 2. The data points shown with asterisks (and error bars) are for the *XMM-Newton* gratings observations from Haberl et al. (2006; for day 5920) and Heng et al. (2008; for day 7269).

and LEG spectra following the standard analysis procedure. We fitted them with our URLP model and recovered the bulk gas velocities with an accuracy within 10% of the input values.

In the simple shock picture, the shock velocities should exceed the bulk velocities by a factor 4/3. But in fact, the postshock temperatures implied by the bulk velocities and Equation (1) are far lower than those inferred from the spectral fits (see Section 3.2). As we discuss in Section 6, this emphasizes the importance of reflected shocks.

4.2. Line Ratios and Light Curves

The X-ray emission line spectrum of shock-heated plasmas is sensitive to ionization age, $n_e t$, as well as postshock temperature. If $n_e t < 10^{13} \text{ cm}^{-3} \text{ s}$, the shocked plasma will be underionized compared with a plasma in coronal equilibrium at the same temperature. Moreover, inner-shell excitation and ionization boost the emission of the forbidden line in the He-like triplets. These effects are discussed in detail by Liedahl (1999), Mewe (1999), and Borkowski et al. (2001).

Following Z05, we analyzed the K_{α} and Ly_{α} spectral lines of the H-like and He-like species of O, Ne, Mg, and Si to determine those regions in the parameter space of electron temperature and ionization age for which the observed line ratios correspond to the values that would result in a plane-parallel shock. As in our analysis of the LETG 2004 observations, we see again that no single combination of electron temperature and ionization age is consistent with all the observed ratios. Therefore, the new

data confirm that the X-ray emission of SNR 1987A comes from a distribution of shocks having a range of ionization ages and postshock temperatures. We also note the overall similarity between the LETG and HETG results for the line ratios of O, Ne, and Mg and the apparent differences for the G-ratios of the silicon He-like triplet. This emphasizes again the importance of spectral resolution for deriving such quantities, e.g., the Si lines are well resolved in MEG (also in HEG) while they are not resolved in LEG (Figure 3).

Up to now, we have acquired dispersed spectra of SNR 1987A with *Chandra* spanning four epochs (Michael et al. 2002; Z05, Z06; D08 and this work), while two additional dispersed spectra have been acquired with *XMM-Newton* (Haberl et al. 2006; Heng et al. 2008). Figure 6 displays light curves of prominent Ly_{α} and K_{α} emission lines from these sources and, in the third column, the ratio of K_{α}/Ly_{α} .⁸

As seen in Figure 6, the light curves of the spectral line fluxes are very similar to the light curve of the total X-ray flux (0.5–2 keV) of SNR 1987A (Park et al. 2006, 2007). Namely, they show a considerable acceleration in brightness during the past few years. A slightly different behavior is evident in the light curves of the line ratios (third column in Figure 6). We see a gradual increase of the ratio of K_{α}/Ly_{α} for the He- and

⁸ Spectral lines with wavelength shorter than $\sim 12 \text{ \AA}$ were not discussed by Haberl et al. (2006) and Heng et al. (2008). The 2007 *XMM-Newton* line fluxes from Heng et al. (2008) were corrected by a factor of 0.461. This correction factor is based on a private communication between D. Dewey, R. McCray, F. Haberl and K. Heng (see Heng et al. 2008).

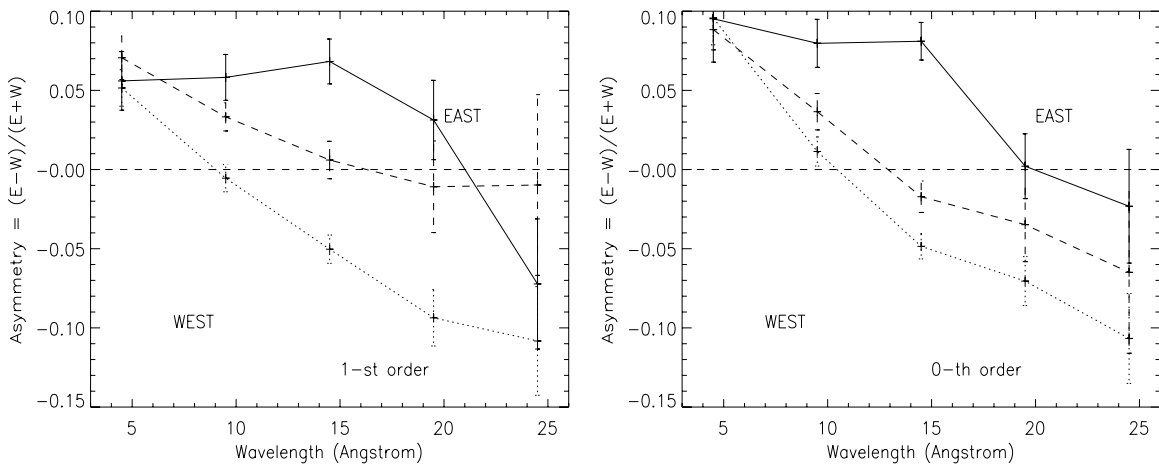


Figure 7. East/west asymmetry in the grating spectra of SNR 1987A measured in the wavelength (energy) intervals: (2–7) Å, (7–12) Å, (12–17) Å, (17–22) Å, and (22–27) Å. Results for LEG 2004, MEG 2007, and LEG 2007 are shown with solid, dashed, and dotted lines, respectively. Results for the first-order spectra are shown in the left panel and those for the zeroth-order spectra are in the right panel.

H-like ions of Si and Mg, while the corresponding ratios remain approximately constant for Ne and O. Keeping in mind that the lines of Si and Mg are emitted from hotter plasmas than those of Ne and O, we note that such a behavior is consistent with our findings from the global fits to the X-ray spectra of SNR 1987A (see Section 3). That is, the average temperature in the high-temperature tail of the shock distribution is decreasing with time while that of the cooler plasma remains approximately constant. The same trend is seen in fits to the pulse-height spectra obtained from the imaging observations (Park et al. 2006).

5. TWO-DIMENSIONAL RESULTS

Since SNR 1987A is spatially resolved by *Chandra*, it is possible to extract spatially resolved spectral information from the grating observations carried out so far. We recall that for each of our observations the instrument configuration was chosen to maximize the outcome from the spatial-spectral effects. Thus, the actual roll angles put the dispersion direction closely along north–south on the sky and the cross-dispersion direction in east–west. Given that the spatial-spectral effects influence the spectra (emission line profiles) mostly in the north–south direction (along the dispersion axis), it is then feasible to extract and analyze the X-ray spectra of the east and west halves of SNR 1987A.

The X-ray spectra from east and west halves can be distinguished by making use of column “tg-d” in the event file of a grating observation. For the data sets in 2007 (MEG and LEG), we used this parameter to obtain event files of the east and west parts for each observation in that data set. Then, we extracted the positive and negative first-order spectra and combined them into a total east and west spectra for the data set at hand. For consistency, we applied the same procedure to the data obtained in 2004 (LEG), although their quality (photon statistics) is lower than that of the 2007 data.

To characterize the east/west asymmetry, we constructed the parameter $A = (E - W)/(E + W)$, where E and W represent the number of X-ray counts in the east and west spectra, respectively. We split the entire spectrum in five wavelength (energy) intervals and measured the asymmetry in each of them. Figure 7 shows the results from this procedure. Similarly, we measured the east/west asymmetry for the zeroth-order spectra, and we display the results in the right panel of Figure 7. A well-established trend with wavelength (energy) is evident. We

emphasize that the actual values for the asymmetry can be affected by the *Chandra* astrometry, but this is not the case for the observed trend. We therefore conclude that the X-ray emission from the eastern half dominates at short wavelengths (high energies), and the opposite is true at long wavelengths (low energies).

In general, high-energy photons come predominantly from hotter plasma (behind faster shocks) while low-energy ones are a sign of relatively cooler plasma (behind slower shocks). In other words, the established east/west asymmetry signifies an asymmetry in the shock distribution in SNR 1987A. To check this, we fitted the east and west spectra for each data set with the two-shock model discussed in Section 3. We held the X-ray absorption and abundances fixed to their best values from our simultaneous global fits to the three data sets under consideration (LEG 2004, MEG 2007, LEG 2007). The results from the fits to the east and west spectra are: (1) the emission measure corresponding to the faster shock is the same for the east and west parts in 2004 while the east half became dominant in 2007 (by 24% in MEG; and by 10% in LEG); (2) the emission measure in the slow shock evolved between 2004 and 2007 as the east part was dominant in 2004 (by 20%) and in 2007, this was true for the west half (by 37% in MEG; and by 25% in LEG); (3) the plasma temperatures for the cooler (slow shock) and hotter (fast shock) components in east and west are within the 1σ range of the values derived from the global fits (see Table 2).

Keeping in mind the uncertainties from the *Chandra* astrometry, we also note that the east–west spectral extraction are not strictly aligned between the three data sets since their effective north–south directions fall within 15° from each other. Nevertheless, the two-dimensional results reported above makes us confident to conclude that the X-ray emitting region in SNR 1987A does show asymmetric shock distribution, with its east part being richer in fast shocks and its west part being richer in slow shocks. This conclusion is consistent with the trend found by Park et al. (2004), who reported differential flux changes of the slow shock component in SNR 1987A between 2000 and 2002. On the other hand, the infrared images of the inner ring in SNR 1987A show that its eastern half dominates the emission in this spectral range (Bouchet et al. 2004, 2006). Since this is thermal emission from dust which is collisionally heated by the hot gas (Bouchet et al. 2004, 2006; Dwek et al.

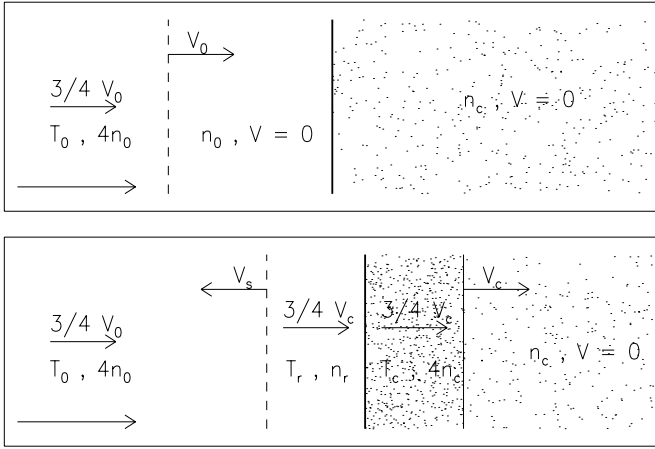


Figure 8. Schematic of the plane-parallel RSS. The postshock velocities and densities have their values for strong shocks with adiabatic index $\gamma = 5/3$. The upper panel shows the situation before the interaction of the “blast” wave (forward shock) with a dense “cloud.” The dashed vertical line denotes the forward shock and the thick solid line denotes the edge of the cloud. The lower panel depicts the situation after the interaction as a transmitted shock and a reflected shock have appeared. Here, positions of the reflected and transmitted shocks are denoted by a dashed and solid line, respectively, while the thick solid line shows the position of the contact discontinuity. The long arrow in the lower left corner in each panel indicates the positive direction of the x -axis.

2008), its spatial distribution traces that of the X-ray emitting plasma. It is then conclusive that the fast shocks may also play an important role in heating the dust in the inner ring, which reemphasizes the importance of a more elaborated modeling of the SNR 1987A emission in different spectral domains.

6. DISCUSSION

The main results from our analysis of the new *Chandra* grating spectra of SNR 1987A are: (1) it is possible to match the overall X-ray spectrum in the framework of a simple shock picture; but (2) the bulk gas velocities inferred from the line profiles are much far less than the velocity that we would expect of gas shocked to the plasma temperature inferred from the spectra.

A number of possible effects might account for a lower difference between the widths of the broadened and narrowed line profiles, which would result in measurements of effective bulk gas velocities that may be less than the actual velocities. For example, (1) an emission line might be contaminated by weak lines due to other species; (2) the shock front might extend to a greater latitude than the 10° assumed in the present model. Such a geometry will give a lower line width for the same bulk velocity; (3) the line emissivity is not uniformly distributed with the azimuthal angle. Moreover, a general caveat regarding our simple picture is that we assume a single bulk gas velocity for each line while in reality, the lines likely form in multiveLOCITY gas flows.

But, as we have suggested (Z05 and D08), we think that the most likely explanation for the discrepancy is that most of the X-ray emitting gas has been shocked twice: first by the blast wave as it overtakes stationary gas and second, by a reflected shock that appears when the blast wave suddenly encounters dense gas in the circumstellar ring. The reflected shock will decelerate the gas that has been shocked by the blast wave and further raise its temperature and density. If this is the case, there will also be a transmitted shock that enters the dense gas. The schematic of such a reflected shock structure (RSS) is shown

in Figure 8. Possibly, the bimodal temperature distribution that we see in the X-ray emitting gas results from a superposition of high-temperature emission from the twice-shocked gas and low-temperature emission from denser gas behind the transmitted shock.

In order to explore this possibility, we have constructed a plane-parallel model for NIE X-ray emission from a blast wave, a transmitted and a reflected shock. Details of the model and its implementation in XSPEC are given in Appendix B. We considered two basic cases for modeling the line profiles in the resultant X-ray spectrum: (1) one that corresponds to Equation (2) (which was originally adopted in Z06 and also used for our two-shock model in Section 3) and (2) a model in which the line profiles correspond to the bulk gas velocities in the RSS convolved with the spatial broadening due to the size of the inner ring (the spatial-spectral effects for a ring with an inclination angle 45° and a small opening angle $\beta = 10^\circ$ are explicitly taken into account as described in Appendix A).

The quality of the RSS model fits with a Gaussian line profile (following Equation (2)) is as good as in our two-shock model and the derived abundances fall within the confidence limits given in Table 1. Therefore, in our actual fits we fixed the abundances to their “best” values from the two-shock model in order to decrease the number of free parameters. The simultaneous fit ($\chi^2/\text{dof} = 1834/2258$) to the entire data set (LEG 2004, MEG 2007, and LEG 2007) gave a column density of $N_H = 1.44 \pm 0.05 \times 10^{21} \text{ cm}^{-2}$ and the following parameters for “average” RSS (transmitted shock, TS; direct shock, “blast” wave, DS; reflected shock, RS):

1. $kT_{\text{TS}} = 0.58 \pm 0.02$, $kT_{\text{DS}} = 2.43 \pm 0.18$, $kT_{\text{RS}} = 3.78 \pm 0.28$ (LEG 2004);
2. $kT_{\text{TS}} = 0.60 \pm 0.01$, $kT_{\text{DS}} = 2.06 \pm 0.09$, $kT_{\text{RS}} = 3.07 \pm 0.13$ (MEG 2007);
3. $kT_{\text{TS}} = 0.59 \pm 0.01$, $kT_{\text{DS}} = 1.74 \pm 0.07$, $kT_{\text{RS}} = 2.50 \pm 0.10$ (LEG 2007).

Temperatures are in keV and the errors are 1σ values from the fit. Emission measures in each of the shocks, relative to that of the direct shock, in the same time sequence are

1. $\text{EM}_{\text{TS}} = 4.7$, $\text{EM}_{\text{DS}} = 1.0$, $\text{EM}_{\text{RS}} = 0.4$ (LEG 2004);
2. $\text{EM}_{\text{TS}} = 4.6$, $\text{EM}_{\text{DS}} = 1.0$, $\text{EM}_{\text{RS}} = 0.6$ (MEG 2007);
3. $\text{EM}_{\text{TS}} = 6.5$, $\text{EM}_{\text{DS}} = 1.0$, $\text{EM}_{\text{RS}} = 1.2$ (MEG 2007).

Thus, we see again that the temperature of the X-ray emitting plasma is on the average decreasing with time, while an increasing amount of plasma is affected by the reflected shocks.

On the other hand, the RSS model in conjunction with the ring kinematics gives a best fit having much lower quality ($\chi^2/\text{dof} = 2708/2260$). The model line profiles are narrower than the observed profiles. We are not surprised: our plane-parallel model is surely an oversimplification. As we have already shown (D08), we can fit the observed profiles of individual lines in the HETG spectrum if we introduce a local Gaussian Doppler broadening in addition to the term representing the bulk velocity of the shocked gas. The complex hydrodynamics (including normal and oblique shocks) that results from the interaction of the blast wave with dense clumps in the ring probably accounts for this extra broadening. Of course, we can improve the quality of the fit to the RSS model if we introduce additional variable parameters. For example, if we add a Gaussian broadening term with the same velocity dispersion for the entire spectrum, the quality of fit improves to $\chi^2/\text{dof} = 1960/2257$, and the

X-ray absorption and plasma parameters (shock temperatures and abundances) reach values similar to those discussed above. We regard the addition of such a Gaussian broadening term as an ad hoc way to allow for the complexity of the actual gas dynamics.

The parameters of the RSS model fit can be used to infer the typical density contrast, n_c/n_0 , between the clumps and their surroundings (the smooth interclump medium) in the inner ring of SNR 1987A (see Appendix B). Namely, the deduced values are $n_c/n_0 = 11.7, 8.8,$ and 6.9 for LEG 2004, MEG 2007, and LEG 2007, respectively. We believe that such a gradual decrease of the inferred density contrast suggests the following picture: as the blast wave penetrates deeper into the environment of the inner circumstellar ring, it encounters interclump gas of steadily increasing density and slows down while the clumps have approximately the same high density. The X-ray emission is increasingly dominated by slow shocks that are transmitted into embedded dense clumps, while shocks reflected from these clumps further compress and heat the gas that was already shocked once by the blast wave. Such a picture is in qualitative accord with the observed temperature evolution of the X-ray emitting plasma (see Section 3). It is also in accord with the decelerating radial expansion of SNR 1987A as deduced from the X-ray images (see Figure 2 in Park et al. 2007) and from the analysis of the X-ray light curve (e.g., Park et al. 2006).

We emphasize that the X-ray spectra and images manifest only part of the complex hydrodynamic interaction of the blast wave with the inner circumstellar ring. The similar morphologies of the optical and soft X-ray images (e.g., McCray 2007) suggest that the shocks responsible for the optical hot spots are related to those responsible for the X-ray emission. However, they are not the same shocks. In their analysis of the optical spectrum of Spot 1, Pun et al. (2002) showed that the optical emission comes from regions of high densities ($n_e \sim 10^6 \text{ cm}^{-3}$), which must result from radiative shocks that can compress the preshock gas by a factor ≥ 100 . Such radiative cooling cannot take place in the hot plasma seen in the X-ray spectra. Taking the standard cooling function of optically thin plasma (Raymond et al. 1976) for plasma temperatures $10^5 \text{ K} \leq T \leq 4 \times 10^7 \text{ K}$, we estimate that the radiative cooling time is $t_{\text{cool}} \approx 270 n_4^{-1} V_{1000}^{3.2} \text{ yr}$, where n_4 is the preshock nucleon number density in units of 10^4 cm^{-3} and V_{1000} is the shock velocity in 1000 km s^{-1} , i.e., much greater than the time since the interaction began. Including effects of NEI may decrease this estimate but not by an order of magnitude.

The spatial correlation of the relatively cool ($T \sim 10^4 \text{ K}$) optical spots and the hotter ($T \geq 10^6 \text{ K}$) X-ray emitting regions indicates that much denser clumps may coexist with less dense ones. The hydrodynamics of such interaction may be quite complex. The optical emission comes from shocks transmitted into the dense clumps by the impact of the blast wave, while the X-ray emission can come both from shocks transmitted into less dense clumps or shocks reflected off the optically emitting clumps. Alternatively, when the blast wave overtakes a clump of intermediate density, the transmitted shock resulting from encounter of the blast wave at nearly normal incidence may be fast enough to heat the plasma to X-ray emitting temperatures, while the transmitted shock resulting from passage of the blast wave around the sides of the clump may be slow enough to undergo radiative cooling and collapse, resulting in the observed optical emission (see Section 4.1 in Pun et al. 2002; also Borkowski et al. 1997). Clearly, we need

continued multiwavelength spectroscopic observations to sort out the real physical picture of the shock interaction in SNR 1987A.

7. SUMMARY

In this work, we presented spectral analysis of the entire data set (LETG and HETG) for SNR 1987A obtained with *Chandra* in 2007. The basic results and conclusions are as follows.

1. Global fits of shock models to the spectra of SNR 1987A show that the average temperature of the X-ray emitting plasma behind the slower shocks has remained nearly stationary for the last few years, while that behind the faster shocks has gradually decreased.
2. Light curves of strong X-ray emission lines and their ratios confirm that the temperature of the high-temperature component of the X-ray emitting gas has decreased.
3. Profiles of the strong emission lines were modeled in two different ways. The results are consistent and show that the deduced bulk gas velocities of the X-ray emitting plasma are too low to account for the observed temperatures in a simple shock model. This result suggests that much of the X-ray emission seen in SNR 1987A comes from gas that has been shocked twice, first by the blast wave and second by shocks reflected off dense clumps (Z05; D08).
4. To explore the reflected-shock scenario in a more quantitative manner, we have developed a new model that assumes a plane-parallel geometry and takes into account the details of NEI. Global fits with this model to the entire 2004–2007 gratings data set show that the contribution from reflected shocks to the X-ray emission from SNR 1987A increases with time. Despite its oversimplification, this model illustrates the general physical picture. It points to more elaborate and realistic models that may result from fits to spectral data spanning evolution of the SNR for several more years.
5. The bulk gas velocities derived from the line profiles seen in the LETG data tend to be larger than those from the HETG data. We attribute this discrepancy to the inferior spectral resolution of the LETG compared with the HETG, and therefore believe that the velocities derived from the HETG data are more accurate, especially, at shorter wavelengths. At wavelengths $\sim \lambda > 18 \text{ \AA}$, the LETG results might be considered more reliable as a result of better photon statistics in the LETG spectra.
6. Two-dimensional analysis of the X-ray grating observations indicates an asymmetry in the shock distribution in SNR 1987A, namely, the east half of the remnant is richer in fast shocks and the west half is richer in slow shocks.

This work was supported by NASA through Chandra grant GO7-8062X to the University of Colorado at Boulder and by contract SV3-73016 to MIT for Support of the Chandra X-ray Center. The authors appreciate the comments of an anonymous referee.

Facilities: CXO (HETG, LETG)

APPENDIX A

UNIFORM RING MODEL FOR LINE PROFILES

The spatially resolved X-ray images of SNR 1987A (e.g., Park et al. 2006) show that the X-ray emission originates in a ringlike

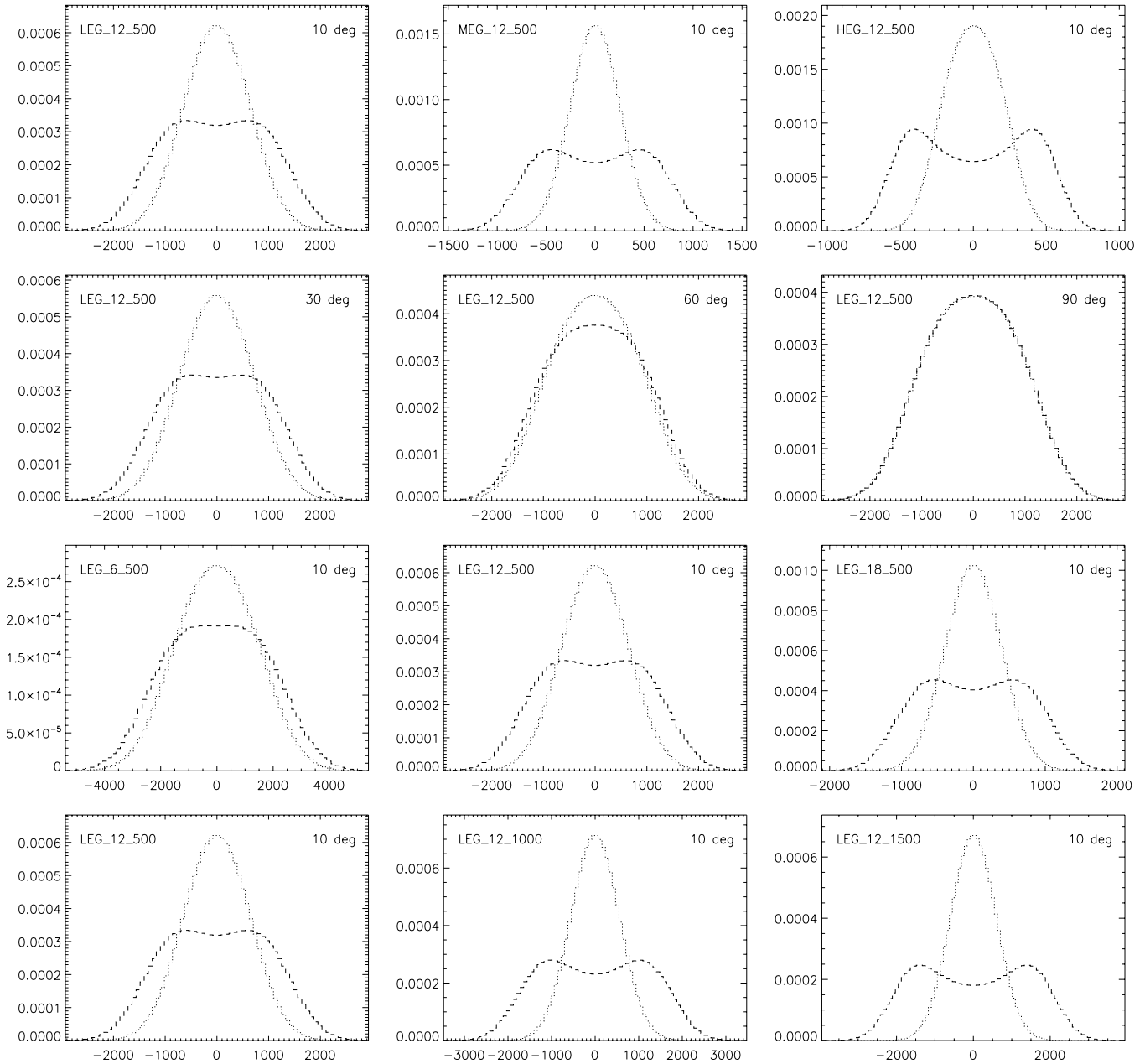


Figure 9. Theoretical line profiles from uniform equatorial ring with inclination angle 45° . Labels in the upper left corner of each panel consecutively indicate the *Chandra* gratings, fiducial line wavelength in \AA , and the bulk gas velocity of the emitting plasma in km s^{-1} . Labels in the upper right corner of each panel indicate the half the opening angle of the equatorial ring. The line profiles are also convolved with a response function (assumed to be a Gaussian) that corresponds to the gratings spectral resolution. The stretched and narrowed line profiles are depicted by dashed and dotted lines, respectively. Horizontal axes are the Doppler velocities (km s^{-1}); vertical axes are the flux densities per km s^{-1} .

structure. On the other hand, the first grating observations of this object with good photon statistics (Z05, Z06) clearly showed that this structure is “flat” (not just a hollow sphere). Thus, it is natural to assume that the X-ray emission of this object originates in a ring with parameters similar to those of the optical inner ring in SNR 1987A.

In our uniform ring model, we assume that the X-ray emitting region is an equatorial section of a spherical shell with inner and outer diameters of $1''.55$ and $1''.7$, respectively, inclination angle of 45° to the observer’s line of sight (LOS), which extends in latitude to an angle $\pm\beta$ that can be adjusted. The X-ray emitting gas is uniformly distributed in the ring and expands radially with a constant velocity. Such an extended object is spatially resolved by *Chandra* so that its spatial extent will be manifested

as equivalent line broadening in the dispersed spectrum. Also, the blue- and redshifted Doppler velocities in different parts of the X-ray emitting region will influence the emission line profile. These spatial-spectral effects⁹ distort the dispersed line images so that the line profiles will be stretched in one of the spectrograph’s arms and compressed in the other one.

In order to take these effects into account, we perform a three-dimensional integration to simulate the theoretical line profiles. For each parcel of gas, we calculate the line-of-sight projection of the radial velocity (or Doppler shift) and the effective wavelength shift (spatial shift) that corresponds to the

⁹ For a general discussion of the spatial-spectral effects see Section 8.5.3 in the *Chandra* Proposer’s Observatory Guide, version 10.

position of this parcel of gas in the geometrical ring. These two terms determine the resultant profile of a given spectral line. Note that the spatial broadening in terms of equivalent Doppler velocities depends both on the wavelength of the emission line and on the spectrometer at hand. The dispersion of the *Chandra* gratings are 0.056 (LEG), 0.0226 (MEG) and 0.0113 Å arcsec⁻¹ (HEG); these map the spatial extent of the ring to quite different equivalent gas velocities if, for example, a spectral line at 6 or 12 Å is observed with each of these instruments.

Figure 9 illustrates the effects of various model parameters on the theoretical line profiles. As expected, when the X-ray emission region does not have a “flat” geometry, for example, if the ring is actually a spherical shell ($\beta = 90^\circ$), the difference between the line profiles in the two arms of the spectrograph vanishes.

We constructed two custom XSPEC models to simulate the spatial-spectral effects for SNR 1987A. The first one explicitly follows the description given above and gives the resultant profiles. The parameters are: the ring’s inner and outer radii, its inclination, and equatorial half opening angle β and the central wavelength of the spectral line, its total flux and the bulk gas velocity. The second model, used to fit the global X-ray spectra, assumes the same geometry but a combination of plane-parallel transmitted and reflected shocks, as discussed in Section 6. Fits based on this model require substantially more computing time in XSPEC than the standard spectral-line broadening models since a three-dimensional integration must be performed for each wavelength bin in the spectrum.

APPENDIX B

REFLECTED SHOCK STRUCTURE

We consider a simplified picture of a reflected shock structure (RSS), in which a blast wave propagates through relatively rarefied (nucleon number density n_0) intercloud gas at constant velocity V_0 and encounters a static dense cloud (density n_c). After the encounter, a shock is transmitted into the dense cloud and a reflected shock begins to propagate backward, further compressing the shocked gas behind the blast wave. We assume plane-parallel geometry, adiabatic shocks, and equal electron and ion postshock temperatures.

The RSS that appears after the interaction has three discontinuities separating plasmas with different characteristics. The unshocked dense gas in the cloud is compressed, heated, and set into motion by the transmitted shock. A contact discontinuity separates this shocked cloud gas from intercloud gas that has been shocked twice. This gas will have the same bulk velocity and pressure as the shocked cloud gas but lower density and higher temperature. Further downstream is the reflected shock, which separates this twice-shocked intercloud gas from intercloud gas that has been shocked once by the blast wave. Figure 8 shows the RSS schematic as the postshock velocities and densities have their values for strong shocks with adiabatic index $\gamma = 5/3$.

The physical parameters in various parts of RSS follow from the standard solutions (velocity, density, and pressure) for a plane-parallel shock:

$$V_2 = \frac{(\gamma - 1)M^2 + 2}{(\gamma + 1)M^2} V_1, \quad \rho_2 = \frac{(\gamma + 1)M^2}{(\gamma - 1)M^2 + 2} \rho_1, \\ P_2 = \frac{2\gamma M^2 - (\gamma - 1)}{\gamma(\gamma + 1)M^2} \rho_1 V_1^2 = \frac{2\gamma M^2 - (\gamma - 1)}{(\gamma + 1)} P_1,$$

where M is the Mach number of the flow ($M^2 = \rho_1 V_1^2 / \gamma P_1$) and subscripts “1” and “2” denote the flow parameters in front and behind the shock front, respectively. Velocities are given in the rest frame of the shock itself; thus, the parameter V_1 represents the actual shock velocity. Taking adiabatic index $\gamma = 5/3$, we find

$$V_2 = \frac{M^2 + 3}{4M^2} V_1, \quad \rho_2 = \frac{4M^2}{M^2 + 3} \rho_1, \quad (B1) \\ P_2 = 3 \frac{5M^2 - 1}{20M^2} \rho_1 V_1^2 = \frac{5M^2 - 1}{4} P_1.$$

In the case of strong shocks ($M \gg 1$), the well-known solution $V_2 = V_1/4$, $\rho_2 = 4\rho_1$, and $P_2 = 3/4\rho_1 V_1^2$ follows.

Since our final goal is to simulate the RSS X-ray emission, in what follows we use the plasma temperature instead of the gas pressure: thus, T_0 , T_r , and T_c denote this parameter behind the blast wave, reflected and transmitted shocks, respectively. We introduce the following dimensionless variables: $x = V_s/V_0$ and $w = V_w/V_0$, where V_s is the velocity of the reflected shock in the observer’s rest frame, and $V_w = 3/4V_c$ is the plasma velocity behind the reflected and transmitted shocks. Using the first formula in Equation (B1), we find that the velocity of the reflected shock is given by

$$V_w - V_s = \frac{M^2 + 3}{4M^2} \left(\frac{3}{4} V_0 - V_s \right), \quad w - x = \frac{M^2 + 3}{4M^2} \frac{3 - 4x}{4}.$$

With the corresponding Mach number for the reflected shock, the variable x can be given as

$$M^2 = \frac{(3 - 4x)^2}{5}, \quad x = \frac{(3 + 8w) - \sqrt{64w^2 - 96w + 81}}{12}. \quad (B2)$$

Thus, for any value of parameter $w \in [0, 3/4]$ we can use Equations (B1) and (B2) to derive the solution for the RSS: $w \rightarrow x \rightarrow M$.

On the other hand, the condition of pressure equality across the contact discontinuity and Equations (B1) give

$$\frac{n_0}{n_c} = \frac{4}{5M^2 - 1} \frac{T_c}{T_0}, \quad (B3) \\ 8x^2 - 4x - 4 + (3 - 4x) \sqrt{\frac{n_0}{n_c} [(3 - 4x)^2 - 1]} = 0.$$

Now for any value of the density contrast $n_0/n_c \in [0, 1]$, Equations (B1) and (B3) give the necessary RSS solution: $n_0/n_c \rightarrow x \rightarrow M$.

Figure 10 shows the RSS solution as function of the density contrast between the cloud and its surroundings. The two limiting cases are worth noting. First, when the blast wave interacts with a very dense cloud ($n_0/n_c = 0$), we find the classical solution of the problem of a shock interaction with a wall (Landau & Lifshitz 1995): $M = \sqrt{5}$, and density and temperature jumps at the reflected shock front by factors 2.5 and 2.4, respectively. The reflected shock velocity has space velocity $V_s = -V_0/2$, i.e., it is moving opposite to the original blast wave with half the blast wave velocity. At the other limit, with no density discontinuity ahead of the blast wave ($n_0/n_c = 1$), the derived Mach number is equal to unity, and no RSS appears. Thus, the basic variable we used for deriving the RSS solution has a range of possible values $x \in [-0.5, \frac{3-\sqrt{5}}{4}]$,

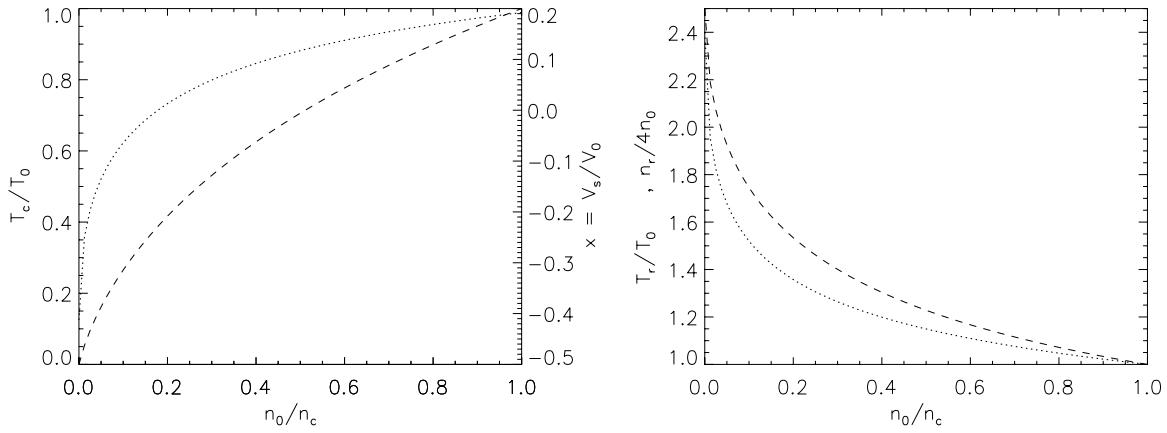


Figure 10. Shock parameters in the reflected shock structure (RSS) as function of the density contrast n_0/n_c . Left panel: the resultant contrast (T_c/T_0 , dashed line) between the temperatures behind the transmitted and forward shock, as well as the velocity (V_s/V_0 , dotted line) of the reflected shock surface in space (the observer’s coordinate system). Right panel: the temperature (T_r/T_0 , dotted line) and density ($n_r/4n_0$, dashed line) jumps behind the reflected shock, having asymptotic ($n_c \gg n_0$) values of 2.4 and 2.5, respectively.

which corresponds to the Mach number of the reflected shock ranging from $M \in [1, \sqrt{5}]$.

To calculate the X-ray emission from the RSS, we need to know the temperature and emission measure of plasma in each zone of the RSS. We recall that for plane-parallel shock the emission measure of the shocked gas is related to the ionization age of the shock, $\tau = n_e t$, namely, $EM \propto n_2 V_2 \tau$. Given that the transmitted and reflected shocks have equal age (they were “born” at the same instant), we find

$$\begin{aligned} \frac{EM_c}{EM_d} &= \frac{5M^2 - 1}{4} \frac{\tau_c}{\tau - \tau_l} \sqrt{\frac{T_0}{T_c}}, \\ \frac{EM_r}{EM_d} &= d_{\text{jump}} \frac{\tau_l}{\tau - \tau_l}, \\ \frac{\tau_l}{\tau_c} &= \frac{4}{5M^2 - 1} \frac{T_c}{T_0} (3 - 4x), \\ \frac{\tau_r}{\tau_l} &= \frac{d_{\text{jump}}}{3 - 4x}, \end{aligned} \quad (\text{B4})$$

where τ and τ_l denote the ionization ages of the blast wave and of the twice-shocked gas, respectively; τ_c and τ_r are the ionization ages of the transmitted and reflected shocks, respectively; $d_{\text{jump}} = n_r/4n_0$ is the density enhancement behind the reflected shock; and EM_d , EM_r , and EM_c respectively denote the emission measure of the hot plasma in the blast wave, reflected shock and the transmitted shock.

The ionization age is an important parameter for simulating the X-ray spectra of shocked gases, which are typically in the state of nonequilibrium ionization (NEI). The ionization ages are slightly different in the three basic RSS regions. The plasma behind the transmitted shock has a standard distribution for its ionization age in $[0, \tau_c]$. The ionization age of the plasma in the blast wave that has not yet interacted with the reflected shock ranges from $[\tau_l, \tau]$. In both cases, the ionization age gradually increases downstream in the flow. On the other hand, the NEI effects are more complicated to characterize in the twice-shocked gas. The gas entering the reflected shock had been shocked already by the blast wave and so its ionization state had evolved from its initial condition. But the reflected shock first interacts with the “youngest” gas behind the blast wave, and this plasma becomes the “oldest” in the doubly shocked region.

With all these considerations at hand, we developed a custom model for XSPEC, which simulates the X-ray emission from an RSS and takes into account the NEI effects. The free parameters of the model are: temperatures (T_0, T_c) and ionization ages (τ, τ_c) of the plasma behind the blast wave and the transmitted shock, respectively; chemical composition; and the total emission measure. We recall that the w parameter is defined for any given pair (T_0, T_c) of temperatures by $w = 3/4(V_c/V_0) = 3/4\sqrt{T_c/T_0}$. From this we obtain solutions of Equations (B2) as well as the emission measures from different RSS regions and a lower limit (τ_l) for the ionization age of the plasma in the blast wave (Equations (B4)). The NEI effects in the blast wave and the transmitted shock are taken into account following the Borkowski et al. (2001) *vpshock* model in XSPEC. We modify this approach for the gas behind the reflected shock to account for the initial NEI plasma evolution following the blast wave passage.

We created two variants of the RSS model in XSPEC. In the first, we handled the line broadening in the same way as described by Z06, that is, we assumed a Gaussian profile with a variable width following Equation (2). In the second variant we consider line profiles produced by a uniform disk (see Appendix A) having individual bulk gas velocities in each RSS region (see Figure 8) that are self-consistently derived in the model.

REFERENCES

- Anders, E., & Grevesse, N. 1989, *Geochim. Cosmochim. Acta*, **53**, 197
- Arnaud, K. A. 1996, in ASP Conf. Ser. 101, *Astronomical Data Analysis Software and Systems*, ed. G. Jacoby & J. Barnes (San Francisco, CA: ASP), 17
- Beuermann, K., Brandt, S., & Pietsch, W. 1994, *A&A*, **281**, L45
- Borkowski, K. J., Blondin, J. M., & McCray, R. 1997, *ApJ*, **477**, 281
- Borkowski, K. J., Lyerly, W. J., & Reynolds, S. P. 2001, *ApJ*, **548**, 820
- Bouchet, P., De Buizer, J. M., Suntzeff, N. B., Danziger, I. J., Hayward, T. L., Telesco, C. M., & Packham, C. 2004, *ApJ*, **611**, 394
- Bouchet, P., et al. 2006, *ApJ*, **650**, 212
- Burrows, D. N., et al. 2000, *ApJ*, **543**, L149
- Dewey, D., Zhekov, S. A., McCray, R., & Canizares, C. L. 2008, *ApJ*, **676**, L131 (D08)
- Dwek, E., et al. 2008, *ApJ*, **676**, 1029
- Gorenstein, P., Hughes, J. P., & Tucker, W. H. 1994, *ApJ*, **420**, L25
- Haberl, F., Geppert, U., Aschenbach, B., & Hasinger, G. 2006, *A&A*, **460**, 811
- Hasinger, G., Aschenbach, B., & Trümper, J. 1996, *A&A*, **312**, L9
- Heng, K., Haberl, F., Aschenbach, B., & Hasinger, G. 2008, *ApJ*, **676**, 361
- Landau, L. D., & Lifshitz, E. M. 1995, *Fluid Mechanics* (2nd ed.; Oxford: Butterworth-Heinemann), 377

- Liedahl, D. A. 1999, in *X-ray Spectroscopy in Astrophysics*, Lecture Notes in Phys. 520, ed. J. van Paradijs & J. A. M. Bleeker (New York: Springer), 189
- Lundqvist, P., & Fransson, C. 1996, *ApJ*, 464, 924
- McCray, R. 2007, in AIP Conf. Proc. 937, *Supernova 1987A: 20 Years After. Supernovae and Gamma-Ray Bursters*, ed. S. Immler, K. W. Weiler, & R. McCray (New York: AIP), 3
- Mewe, R. 1999, in *X-ray Spectroscopy in Astrophysics*, Lecture Notes in Phys. 520, ed. J. van Paradijs & J. A. M. Bleeker (New York: Springer), 189
- Michael, E., et al. 2002, *ApJ*, 574, 166
- Park, S., Burrows, D. N., Garmire, G. P., McCray, R., Racusin, J. L., & Zhekov, S. A. 2007, in AIP Conf. Proc. 937, *Supernova 1987A: 20 Years After. Supernovae and Gamma-Ray Bursters*, ed. S. Immler, K. W. Weiler, & R. McCray (New York: AIP), 43
- Park, S., Burrows, D. N., Garmire, G. P., Nousek, J. A., McCray, R., Michael, E., & Zhekov, S. A. 2002, *ApJ*, 567, 314
- Park, S., Zhekov, S. A., Burrows, D. N., Garmire, G. P., & McCray, R. 2004, *ApJ*, 610, 275
- Park, S., Zhekov, S. A., Burrows, D. N., & McCray, R. 2005, *ApJ*, 634, L73
- Park, S., Zhekov, S. A., Burrows, D. N., & McCray, R. 2006, *ApJ*, 646, 1001
- Pun, C. S. J., et al. 2002, *ApJ*, 572, 906
- Raymond, J. C., Cox, D. P., & Smith, B. W. 1976, *ApJ*, 204, 290
- Russel, S. C., & Dopita, M. A. 1992, *ApJ*, 384, 508
- Staveley-Smith, et al. 1992, *Nature*, 355, 147
- Staveley-Smith, et al. 1993, *Nature*, 366, 136
- Sugerman, B. E. K., Lawrence, S. S., Crotts, A. P. S., Bouchet, P., & Heathcote, S. R. 2002, *ApJ*, 572, 209
- Zhekov, S. A., McCray, R., Borkowski, K. J., Burrows, D. N., & Park, S. 2005, *ApJ*, 628, L127 (Z05)
- Zhekov, S. A., McCray, R., Borkowski, K. J., Burrows, D. N., & Park, S. 2006, *ApJ*, 645, 293 (Z06)